

Numerical Investigation on Longitudinal Stage Separation of Spiked Two-Stage-to-Orbit Vehicle

Yue Wang,^{*} Yunpeng Wang,[†] Chun Wang,[‡] and Zonglin Jiang[§]
Chinese Academy of Sciences, 100190 Beijing, People's Republic of China

<https://doi.org/10.2514/1.A35390>

A longitudinal stage separation (LSS) scheme for a parallel-arrangement two-stage-to-orbit (TSTO) vehicle is proposed and analyzed in detail, in which the orbiter moves along the upper surface of the booster. A TSTO concept comprising a waverider and a spaceplane was designed to numerically investigate the dynamic characteristics of the LSS at Mach 7. The influence of spike models assembled at the nose of the orbiter on the LSS at different angles of attack (AoA) (i.e., spike with half cone, spike with half cone-disk, and hemispheric spike) was explored. Moreover, the aerodynamic interference and characteristics were analyzed and compared for different spiked configurations. The aerodynamic interference during LSS is simple and weak, which is only associated with type VI shock/shock interaction, with rapid increases in the axial force when the shock waves of both stages converge. Furthermore, the model with a half cone spike has the best performance in drag reduction by 7%, whereas the model with a half cone-disk spike has the worst performance that increases axial force. The TSTO model with a half cone spike at AoA = 0 and 5 deg is advantageous in LSS because of the high drag reduction and weak aerodynamic interference.

Nomenclature

A	=	axial force, N
AoA	=	angle of attack, deg
C_A	=	axial force coefficient
C_f	=	skin friction coefficient
C_M	=	pitching moment coefficient
C_N	=	normal force coefficient
C_p	=	pressure coefficient
DR	=	nondimensional drag reduction
d	=	height of the stage, m
dt	=	dimensional time step, s
E, H	=	total energy and total enthalpy per unit mass, $J \cdot kg^{-1}$
F_c	=	convective fluxes
F_T	=	thrust on the orbiter, N
F_v	=	viscous fluxes
g	=	gravitational acceleration, $9.8 m \cdot s^{-2}$
h	=	height of interstage clearance, m
I_{xx}	=	moment of inertia about X axis, $kg \cdot m^2$
I_{yy}	=	moment of inertia about Y axis, $kg \cdot m^2$
I_{zz}	=	moment of inertia about Z axis, $kg \cdot m^2$
k_T	=	coefficient of thermal conductivity, $W \cdot (m \cdot K)^{-1}$

L/D	=	ratio of spike length to model base diameter
l	=	length of the stage, m
l_T	=	thrust action stroke, m
Ma	=	Mach number
M_z	=	pitching moment about the center of gravity of stage, $N \cdot m$
m	=	mass, kg
N	=	normal force, N
p	=	pressure, Pa
Re	=	Reynolds number
T	=	temperature, K
U	=	speed, $m \cdot s^{-1}$
u, v, w	=	velocity components in x, y , and z directions, $m \cdot s^{-1}$
V_g	=	contravariant velocity vector at the surface of the control volume, $m \cdot s^{-1}$
V_r	=	contravariant velocity vector relative to the motion of the grid, $m \cdot s^{-1}$
W	=	vectors of conservative variables
w	=	span of the stage, m
x	=	coordinate in the X direction, m
y^+	=	nondimensional wall spacing
γ	=	specific heat ratio
Δx	=	displacement of the orbiter, m
Θ	=	heat conduction, $W \cdot m^{-2}$
μ	=	coefficient of viscosity, $N \cdot s \cdot m^{-2}$
ρ	=	density, $kg \cdot m^{-3}$
$\tau_{i,j}$	=	component of viscous stress, $N \cdot m^{-2}$
ϕ	=	diameter of the rod, mm
ψ	=	angle from the stagnation point of the hemisphere body, deg

Subscripts

b	=	booster conditions
CG	=	center of gravity
iso	=	isolated conditions
o	=	orbiter conditions
s	=	spiked conditions
∞	=	freestream conditions

I. Introduction

TWO-STAGE-TO-ORBIT (TSTO) vehicle may be considered one of the next-generation space transport systems, and it has been widely investigated in the past few decades [1–7]. The generic

Received 12 February 2022; revision received 21 July 2022; accepted for publication 3 August 2022; published online 23 August 2022. Copyright © 2022 by the American Institute of Aeronautics and Astronautics, Inc. All rights reserved. All requests for copying and permission to reprint should be submitted to CCC at www.copyright.com; employ the eISSN 1533-6794 to initiate your request. See also AIAA Rights and Permissions www.aiaa.org/randp.

^{*}Doctoral Student, State Key Laboratory of High-Temperature Gas Dynamics, Institute of Mechanics; also School of Engineering Sciences, University of Chinese Academy of Sciences, 100049 Beijing, People's Republic of China.

[†]Associate Professor, State Key Laboratory of High-Temperature Gas Dynamics, Institute of Mechanics; also School of Engineering Sciences, University of Chinese Academy of Sciences, 100049 Beijing, People's Republic of China; wangyunpeng@imech.ac.cn. Member AIAA (Corresponding Author).

[‡]Professor, State Key Laboratory of High-Temperature Gas Dynamics, Institute of Mechanics; also School of Engineering Sciences, University of Chinese Academy of Sciences, 100049 Beijing, People's Republic of China. Member AIAA.

[§]Professor, State Key Laboratory of High-Temperature Gas Dynamics, Institute of Mechanics; also School of Engineering Sciences, University of Chinese Academy of Sciences, 100049 Beijing, People's Republic of China. Associate Fellow AIAA.

TSTO vehicle consists of a booster with airbreathing combined propulsions and an orbiter with the rocket-power engine, with a parallel arrangement instead of a tandem arrangement to improve its efficiency [8,9]. However, the separation of the parallel-arrangement TSTO stage usually occurs in the hypersonic flow regime, and strong aerodynamic interferences such as shock/shock and shock/boundary-layer interactions (SSI and SBLI) are introduced between stages. The strong aerodynamic interference that could cause a high risk of separation failure is not expected in hypersonic stage separation for TSTO.

The separation scheme determines the effect of the stage separation and relates to the safety of the vehicle. For a long time, the transverse stage separation (TSS) was discussed and studied in the stage separation for parallel TSTO system in the conceptual design or fundamental research using static and dynamic methods. Decker [10] performed an experimental aerodynamic interference study of simple TSTO aerodynamic configurations at Mach 3 and 6. The results showed that interstage interference plays a role in the separation maneuver of TSTO. Moelyadi et al. [11] studied the aerodynamic interferences and characteristics of TSTO with different two-stage relative positions at different Mach numbers. The results showed that mutual interferences were caused by the incident and reflected shock waves and expansion waves. Bordelon et al. [12] conducted wind tunnel tests on the NASA-designed Langley Glide-Back Booster (LGBB) TSTO model. The measured data indicated that the TSTO vehicle is statically unstable due to strong bow shock interactions at several separation positions. Murphy et al. [13] and Murphy and Scallion [14] developed experimental tools and testing methods to address the supersonic and hypersonic stage separation problems for future multistage launch vehicle systems. A large aerodynamic database of the LGBB configuration was obtained through wind tunnel tests, and the aerodynamic data generated in those tests showed excellent agreement with the computational predictions. To reduce aerodynamic interference for TSTO supersonic separation, Uematsu et al. [15–17] conducted aerodynamic interference experiments with different cross sections for simplified LGBB configurations. The results demonstrated that the triangular cross section of the booster has a good reduction effect on the shock wave interactions. Ozawa et al. [18,19] conducted wind tunnel tests on aerodynamic interferences of a hemisphere-cylinder/flat-plate TSTO configuration with various interstage clearances at Mach 8.1. The results showed that the interstage clearance significantly influences the flowfield pattern, heat flux, and pressure on the wall. Jia et al. [20] numerically studied the aerodynamic characteristics of a TSTO model with different nose configurations in the orbiter by analyzing the pressure and heat flux distribution on the wall. The SSI outside the blunt nose of the orbiter causes serious aerodynamic and thermal problems at the stagnation point. Cheng et al. [21] conducted an aerothermodynamics study of TSTO. They found that the interstage complex shock structure and SBLIs are responsible for the considerable increase in aerothermal loads at reflected shock positions.

In terms of dynamic stage separation for TSTO, research is limited due to the complexity and difficulty relative to the static aerodynamic interference, and computational fluid dynamics (CFD) is regarded as a major research method. Brenner [22] performed a dynamic inviscid simulation of TSTO in relative motion. This study revealed a slow transient aerodynamic interference during separation. Cvrlje et al. [23] simulated the unsteady flow of the TSTO model during stage separation at Mach 6.8 and investigated the stability of the TSTO vehicle. They found that the instability could not be neglected in the stability and control evaluations of lateral motion. Liu et al. [24] numerically investigated the aerodynamic interference and stage separation of the TSTO model with turbine-based combined cycle (TBCC) engine. The results showed that changing flap predeflection has a limited effect on improving the safety of stage separation, and a safe separation can be achieved at the angle of attack (AoA) of -2° . Wang et al. [25] stimulated the TSS of a simple TSTO aerodynamic configuration at different angles of incidence at Mach 7. Moreover, the shock structure and separated flow were analyzed, as well as the mechanism of the aerodynamic interference during separation. The analysis demonstrated that the intensity of interstage interference increases with the

increase of incidence angle and decreases with interstage clearance during separation. The incidence angle of $6\text{--}8^\circ$ could be conducive to the safe separation of the TSTO model. In addition to CFD numerical simulation for TSTO separation, NASA studies conducted by Pamadi et al. [26] on the development of “ConSep” simulation tool, an industry-standard package based on MATLAB for solving multibody dynamic problems. Pamadi et al. [26] discussed the application of ConSep to the simulation and analysis of stage separation of TSTO vehicles at Mach 3 and 6 based on the wind-tunnel test aerodynamic database. The effects of parametric variations at staging were evaluated, and Monte Carlo analysis was performed for Mach 3 staging to evaluate the sensitivity of uncertainties in aerodynamic coefficients.

Most previous studies on stage separation for the TSTO model mainly focused on the TSS scheme and revealed that the strong aerodynamic interference exists between stages during TSS. Therefore, steep and complex aerodynamics variation during TSS may induce the stage to recontact and increase the failure risk for TSTO vehicles. Hence, the safe TSS condition of two stages is usually specialized and strict. However, the longitudinal stage separation (LSS) scheme, which is usually applied in tandem multi-stage vehicles, has not gained interest in the paralleled two-stage vehicle staging research to date. In the LSS scheme, in which the orbiter axial separates along the back of the booster with a small clearance, may result in a weaker aerodynamic interference and benefit the safe separation of parallel TSTO vehicle. Hence, the mechanism of flowfield and aerodynamic interference between stages during LSS were revealed and analyzed for the objective of fundamental research in the current study. For this purpose, the simplified assumption of Mach 7 staging of reference TSTO systems was considered: a waverider and a wing-body vehicle are taken as booster and orbiter, respectively. Detailed TSTO system analyses were not addressed. The flowfield and aerodynamics characteristics were numerically analyzed using coupled methods of CFD and six-degree-of-freedom (6-DOF) rigid-body dynamics (RBD). The drag reduction for the orbiter and aerodynamic interference during LSS were addressed by variation of spike models [27–29] and AoA. The other issues on the effects of LSS were not addressed in the current study.

II. Spiked TSTO Configuration and LSS Description

The TSTO concept proposed in this work has horizontal takeoff and landing capabilities. Based on the cone-derived waverider configuration, the booster concept was designed as a wide-speed range vehicle with a deformable wing and double vertical tails. The orbiter is designed as a large swept wing-body with a fairing on the blunt nose. The fairing plays a role in reducing the wave drag of the TSTO, and it is detached during descent so that the orbiter can aerodynamically decelerated with a blunt nose. Figure 1 presents the flight profiles of the reference TSTO systems. The chosen flight point is that the stage separation starts at around Mach 7 and at an altitude of 37 km. For TSTO propulsion systems, the booster is powered by a turbojet/ramjet combined

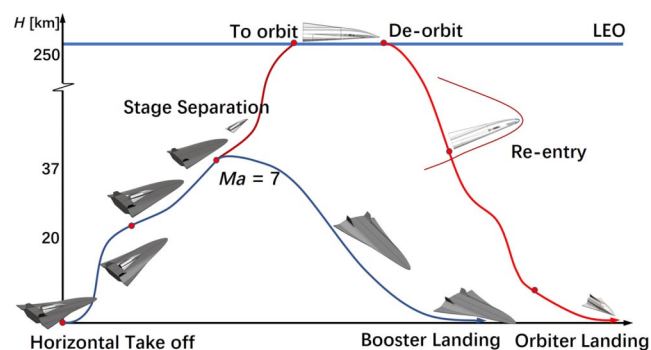


Fig. 1 Schematic illustration of staging flight profile for TSTO systems.

airbreathing propulsion engine, and the orbiter is powered by a rocket engine. The proper operating regimes for the turbojet are about Mach 0–3, and for the ramjet they are about Mach 3–7. Hence, the recommendation staging Mach number is about 7 for the reference TSTO systems under the limitations of the engine operation modes, e.g., the Mach number of stage separation for SANAGER [30] TSTO concept is around at 6.7. Since such proper and recommended staging Mach number for TSTO is proposed, the variations of the stage separation flight conditions are not addressed except for the AoA in this paper. In addition, the full scale of the reference TSTO systems is as follows: the reference body length of the booster in the symmetry plane is 75 m, the length of the orbiter is 30 m, and the scaled model for the numerical simulation is zoomed out 1/75 times. Figure 2a presents a schematic illustration of the scaled TSTO concept without spike, with the XOY plane being the longitudinal plane of the vehicle, and the origin of the coordinate is at the nose of the booster. The length of the booster is $l_b = 1$ m, and the center of gravity (CG) is located at $(0.65, -0.04, 0)$ m, which is about 65% of its length. The length of the orbiter is $l_o = 0.4$ m, and the CG is located at $(0.64, 0.017, 0)$ m, which is about 67% of its length. The minimum interstage clearance is $h/l_b = 0.001$.

Figure 2b shows the schematic of the LSS for the current TSTO stage separation study. LSS means the acceleration of the orbiter at the back of the booster with the rocket power thrust F_T along the flight direction. In addition, the longitudinal displacement of the orbiter, i.e., Δx shown in Fig. 2b, means the displacement of the orbiter's CG in the flight direction (i.e., negative direction of X axis in simulation) during LSS. It is a central notion and key variable in results discussion. The thrust magnitude is $F_T/m_o g = 335$ with a stroke length of $l_T/l_b = 0.03$ (the thrust is set to a high value in order to reduce the simulation time of LSS). The nondimensional mass of the orbiter is $m_o/\rho_\infty l_o^3 = 3125$, and the moments of inertia are $I_{xx}/\rho_\infty \cdot l_o^5 = 22$, $I_{yy}/\rho_\infty \cdot l_o^5 = 203$, and $I_{zz}/\rho_\infty \cdot l_o^5 = 191$, respectively. Herein, ρ_∞ refers to the density of freestream. Moreover, the booster is assumed to be fixed during LSS, and the orbiter is subjected to 6-DOF motion equations. The moment reference point is located to the CG.

Various spike configurations were investigated in this study. Figure 2c presents a schematic illustration of the different spike configurations, where A indicates no spike, B represents spike with half cone, C shows spike with half cone-disk, and D indicates hemispherical spike. Model B utilizes a half cone on its nose, model C utilizes a half cone-disk on its nose, and model D only has a simple stick configuration. These spikes have the same length of $l_s/w_o = 0.75$ and diameter of $\phi/d_o = 0.077$, and more parameters and details are shown in Fig. 2c. Besides, it is assumed that the light spike

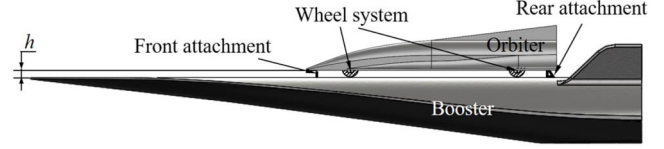


Fig. 3 Schematic illustration of the attachment of the booster and the orbiter.

model does not affect the mass characteristics of the orbiter. Dynamic simulations of three spiked TSTO configurations and the original configuration without spike implemented in LSS at different values of AoA (i.e., 0, 5, and 8 deg) are analyzed in the following sections.

The schematic diagram of the attachment of the orbiter to the booster is shown in Fig. 3 (the clearance between stages is exaggerated for clear presents). The orbiter is attached to the booster at two points and by a wheel system. Before the release, the two joints are assumed to be a fixed support and to integrate two stages. At separation, the attachments have been unlocked and taken back or discarded, and the orbiter operates at full thrust and moves along the upper surface of the booster by the wheel system. The wheel system is retracted into the orbiter fuselage after the separation, and the gear door will reset so that no gap and open volume in the lower surface of the orbiter fuselage, the potential high thermal loads may be avoided. These attachments and systems are similar to the space shuttle and external tank attachment system. Besides the wheel system scheme, another scheme with the sliding track placed on the booster for parallel staging might be feasible too. The attachments and wheel systems between stages, as well as rocket engines, are not included in the numerical simulation, and their effects on the LSS are not addressed.

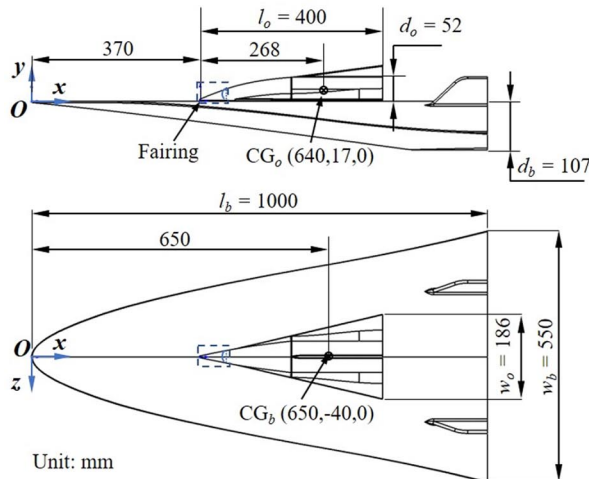
III. Numerical Methods and Validation

A. Governing Equations and Algorithms

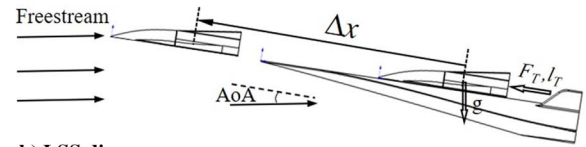
The three-dimensional (3-D) compressible Navier–Stokes equations were employed for the unsteady simulations of stage separation for TSTO:

$$\frac{\partial}{\partial t} \iiint_{\Omega} W d\Omega + \oint_{\partial\Omega} (F_c - F_v) dS = 0 \quad (1)$$

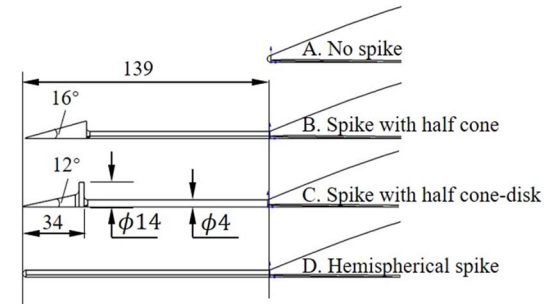
where W , F_c , and F_v are the vectors of conservative variables, convective fluxes, and viscous fluxes, respectively, which are expressed as



a) Overall sizing for the TATO vehicle



b) LSS diagram



c) Spike configuration

Fig. 2 Spiked TSTO configuration and LSS schemes in the present study (unit: mm).

$$\begin{aligned}
W &= \begin{pmatrix} \rho \\ \rho u \\ \rho v \\ \rho w \\ \rho E \end{pmatrix}, \quad F_c = \begin{pmatrix} \rho V_r \\ \rho u V_r + n_x p \\ \rho v V_r + n_y p \\ \rho w V_r + n_z p \\ \rho H V_r + V_g p \end{pmatrix}, \\
F_v &= \begin{pmatrix} 0 \\ n_x \tau_{xx} + n_y \tau_{xy} + n_z \tau_{xz} \\ n_x \tau_{yx} + n_y \tau_{yy} + n_z \tau_{yz} \\ n_x \tau_{zx} + n_y \tau_{zy} + n_z \tau_{zz} \\ n_x \Theta_x + n_y \Theta_y + n_z \Theta_z \end{pmatrix} \quad (2)
\end{aligned}$$

where ρ represents density; u , v , and w represent velocity components in x , y , and z directions, respectively; p represents pressure; and E and H represent total energy and total enthalpy per unit mass, respectively. Furthermore, $p = (\gamma - 1)[\rho E - 1/2\rho(u^2 + v^2 + w^2)]$ and $H = E + p/\rho$, where γ denotes the specific heat ratio; τ_{ij} represents the component of viscous stress; Θ_x , Θ_y , and Θ_z express the heat conduction; n_x , n_y , and n_z represent the components of unit outward-facing normal vector; and V_r represents the contravariant velocity relative to the motion of the grid, which is expressed as

$$V_r = V - V_g = (u - u_g)n_x + (v - v_g)n_y + (w - w_g)n_z \quad (3)$$

where $V_g = u_g n_x + v_g n_y + w_g n_z$ is the contravariant velocity at the surface of the control volume. To close the system of equations, the ideal gas equation of state is introduced: $p = \rho RT$. In addition,

$$\Theta_x = u\tau_{xx} + v\tau_{xy} + w\tau_{xz} + k_T \frac{\partial T}{\partial x} \quad (4)$$

$$\Theta_y = u\tau_{yx} + v\tau_{yy} + w\tau_{yz} + k_T \frac{\partial T}{\partial y} \quad (5)$$

$$\Theta_z = u\tau_{zx} + v\tau_{zy} + w\tau_{zz} + k_T \frac{\partial T}{\partial z} \quad (6)$$

where k_T is the coefficient of thermal conductivity and T is the temperature. The components of the viscous stress tensor are obtained from the following relations:

$$\tau_{xx} = 2\mu \frac{\partial u}{\partial x} - \frac{2}{3}\mu \left(\frac{\partial u}{\partial x} + \frac{\partial v}{\partial y} + \frac{\partial w}{\partial z} \right) \quad (7)$$

$$\tau_{yy} = 2\mu \frac{\partial v}{\partial y} - \frac{2}{3}\mu \left(\frac{\partial u}{\partial x} + \frac{\partial v}{\partial y} + \frac{\partial w}{\partial z} \right) \quad (8)$$

$$\tau_{zz} = 2\mu \frac{\partial w}{\partial z} - \frac{2}{3}\mu \left(\frac{\partial u}{\partial x} + \frac{\partial v}{\partial y} + \frac{\partial w}{\partial z} \right) \quad (9)$$

$$\tau_{xy} = \tau_{yx} = \mu \left(\frac{\partial u}{\partial y} + \frac{\partial v}{\partial x} \right) \quad (10)$$

$$\tau_{xz} = \tau_{zx} = \mu \left(\frac{\partial u}{\partial z} + \frac{\partial w}{\partial x} \right) \quad (11)$$

$$\tau_{yz} = \tau_{zy} = \mu \left(\frac{\partial v}{\partial z} + \frac{\partial w}{\partial y} \right) \quad (12)$$

where μ is the viscosity coefficient, which is evaluated by Sutherland's law [31].

The two-equation Menter shear stress transport (SST) k - ω turbulence model [32] describes the turbulence. Two additional transport

equations are added to the above system, one for the evolution of k and one for ω . For such a linear model, the viscosity in the above equations is written as $\mu + \mu_t$, and the thermal conductivity as $k + k_t$, where μ_t is the coefficient of turbulence viscosity and k_t is the coefficient of turbulence thermal conductivity, $k_t = c_p \mu_t / Pr_t$. The SST k - ω turbulence model is a combination of the k - ω turbulence model in the near wall and the standard k - ω turbulence model in the separation zone. Moreover, it accounts for turbulent shear layer transport in the definition of turbulent viscosity. In addition, the model is less sensitive to the specification of the freestream turbulence level compared to the standard k - ω turbulence model, and it exhibits good performance in calculating the flowfield with adverse pressure gradient. These features makes the SST k - ω turbulence model more accurate and reliable for a wide class of flows, and it has been reported that this model can better predict the flow separation characteristics caused by shock [21,33]. Hence, it is used for describing the turbulence calculation in this paper.

In the current study, the RANS equations are solved by the cell-vertex finite volume method. The numerical flux is evaluated using a second-order total variation diminishing (TVD) scheme based on Harten–Lax–van Leer contact (HLLC) approximate Riemann solver with the minmod limiter [34–36]. The time advancement is performed by implicit backward Euler integration with multigrid acceleration and dual time-stepping methods [37]. To obtain time-accurate results, the nondimensional time step is set to be $dt \cdot U_\infty / l_b = 0.1065$, where dt is the dimensional time step and $U_\infty = 2130 \text{ m} \cdot \text{s}^{-1}$ denotes the freestream speed. The nonslip adiabatic wall condition is adopted for the wall, and the flow variables on the outflow boundary are centroidal extrapolated from the computational domain. The freestream conditions are adopted for the inflow boundary, as $Ma_\infty = 7$, $Re_\infty = 8.61 \times 10^5 \text{ m}^{-1}$, $p_\infty = 392 \text{ Pa}$, and $T_\infty = 228 \text{ K}$. Moreover, the variation of the AoA is achieved by changing the components of the inflow velocity. The dynamic overset grids technique [38] is also used, and the relative position of the orbiter is updated by advancing the 6-DOF motion equations solved by the fourth-order Runge–Kutta method.

B. Dynamic Overset Grid and Grid Independence Study

Due to the advantages of the overset grid technique in dealing with the multibody relative motion problems [38,39], this technique is adopted to compute the dynamic separation of the TSTO vehicle. As shown in Fig. 4a, the 3-D computational grid is composed of a booster grid and an orbiter grid. Both grids are created based on a hybrid meshing approach. Hybrid grids contain structured and unstructured blocks, including hexahedral, prismatic, and tetrahedron cell types. With a boundary-layer grid for the area near the wall, the first cell spacing normal to the wall is chosen to ensure an average $y^+ \sim 1$ to capture an appropriate boundary-layer flow. A progression ratio of approximately 1.1 is applied to cluster grid points radially outward from the wall, and typically 30–40 cells spanned the maximum thickness of the boundary layer.

In terms of overset grid technique, the grids are connected by hole cutting and data interpolation, as shown in Figs. 4b and 4c. The outer boundary of the orbiter grid is set as the cutter boundary, and the cells intersecting the cutter boundary are identified as the cutter cells. Then, the cell of the booster grid inward the cutter cell is cut off, forming the inner boundary of the booster grid. In this way, the cutter and inner boundary form the overset area of two subgrids. Afterward, the flow data are exchanged and interpolated on the overset grids to achieve second-order accuracy within two or more layers of interpolated grid points. More details of the construction steps of the overset grid technique can be found in the study of Tian et al. [38]. When the relative positions of the two stages are updated, the subgrid follows without changing the mesh and produces the overset grid at the very time step. The flow data are exchanged between subgrids to complete the entire flowfield computation for this time step.

In the current study, three grids with different resolutions are used to verify the grid independence. The three grid numbers are coarse grid, medium grid, and fine grid, with the total number of two subgrid cells being around 6 million, 14 million, and 23 million, respectively.

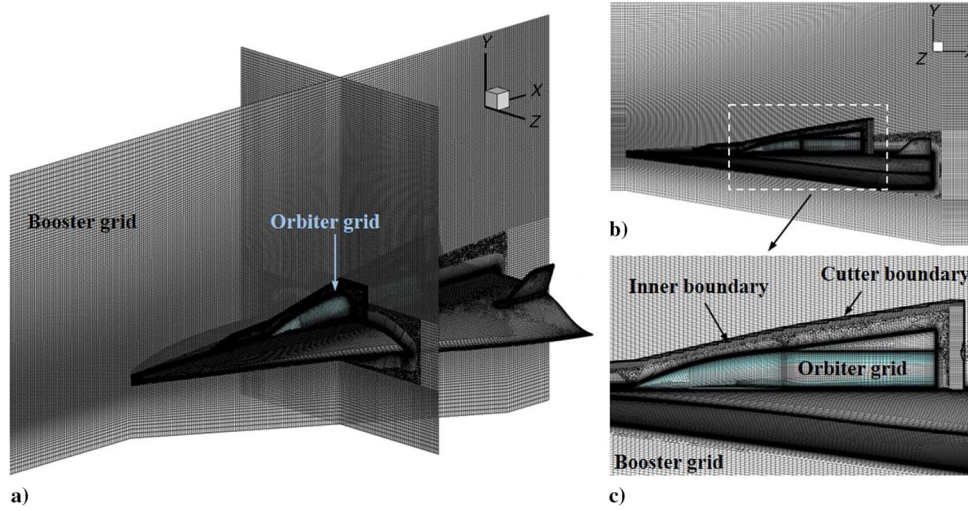
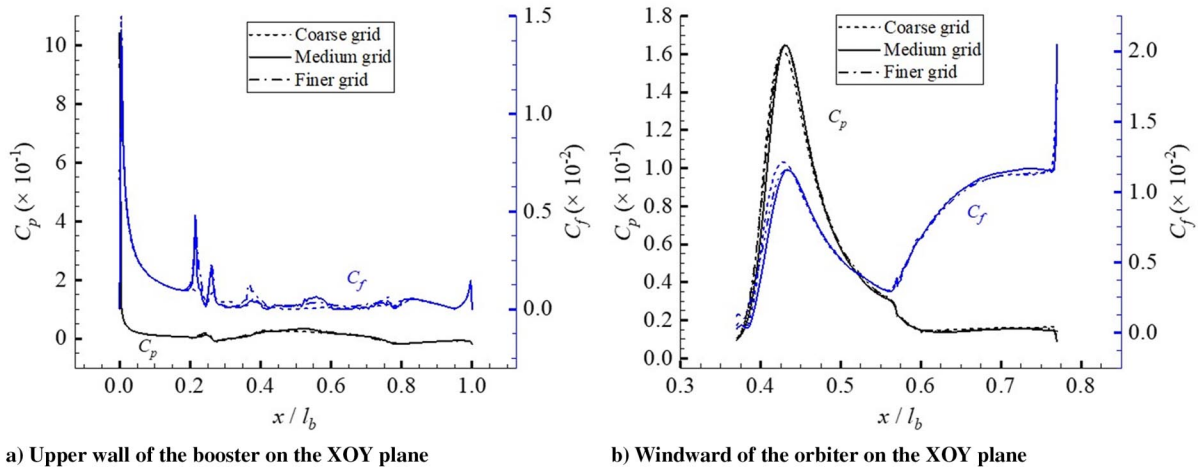


Fig. 4 Overset grid used in the study.



a) Upper wall of the booster on the XOY plane

b) Windward of the orbiter on the XOY plane

Fig. 5 Pressure coefficient and skin friction coefficient distributions on the TSTO vehicle computed from the three grids.

Figure 5 shows the pressure coefficient and skin friction coefficient distributions on the windward side of the orbiter and the upper wall of the booster on the XOY plane of TSTO model B for $AoA = 0^\circ$ before separation. The pressure coefficient and skin friction coefficient curves are approximately the same for all three grids. Besides, the medium and fine grids are more consistent at feature points. To ensure the accuracy and efficiency of computations, the medium grid is selected for the subsequent study and discussion. The computation cost for all cases in the current study is approximately 200 thousand core-hours of the supercomputer at the Beijing Super Cloud Computing Center and Guangzhou Tianhe-2.

C. Validation

In this section, numerical simulations of two classes of a spike in hypersonic flow and the 3-D wing-pylon-store separation are considered to validate the numerical method. Because the spike nose configuration is applied in the current TSTO vehicle study, accompanied by the flow separation and SBLI, it is reasonable to perform the validation. The numerical simulation result considering the SST turbulence model is compared with the experiment of two different spike nose configurations in the study of Motoyama et al. [40]. The spikes in hypersonic flow with $Ma = 7$ and $Re = 4.0 \times 10^5 \text{ m}^{-1}$ are experimentally studied. Figure 6 presents the numerical schlieren flowfield and pressure distribution on the hemisphere body of CFD and experimental results. As shown in Fig. 6, on the one hand, a pressure discrepancy between CFD and measured data exists for the hemispherical nose aerospike in the ψ range $[30^\circ\text{--}45^\circ]$ due to a

transitional separated/reattached flow region, but the variation tendency of the pressure distributions between CFD and experiment is consistent. On the other hand, the computed pressure distribution on the hemispherical body agrees well with the test data in hemispherical aerodisk case.

The wing-pylon-store separation is one of the standard experiment cases to verify the numerical simulation capability of the multi-body relative motion. Based on the dynamic overset grid technique, the inviscid supersonic flow of 3-D wing-pylon-store dynamic separation is computed by coupling the 6-DOF motion equations. The freestream conditions are $Ma = 1.2$, and $Re = 7.87 \times 10^6 \text{ m}^{-1}$, and $AoA = 0^\circ$. The basic geometries are shown in Fig. 7a, the store mass is 907.8 kg, and its moments of inertia are $I_{xx} = 27.12 \text{ kg} \cdot \text{m}^2$ and $I_{yy} = I_{zz} = 100 \text{ kg} \cdot \text{m}^2$, and other details are described in the study of Heim [41] and Snyder et al. [42]. Figure 7b shows the computational hybrid grid with 8.5 million elements. The displacements of the store during separation are shown in Figs. 7c and 7d. As shown in Figs. 7c and 7d, the computational pitching angle (y-Euler angle) and yaw angle (z-Euler angle) are in good agreement with the experimental results [41], but a discrepancy is observed for $t > 0.35 \text{ s}$ for the roll angle (x-Euler angle) values between the simulation and experiment. The reason for the discrepancy may be that the moment of inertia (I_{xx}) of the store in the rolling direction is smaller compared to other moments of inertia (I_{yy} and I_{zz}), and the computation error may be amplified. Overall, the numerical method can accurately simulate the separation process of the store. Through the above two tests, it can be determined that the method in the current

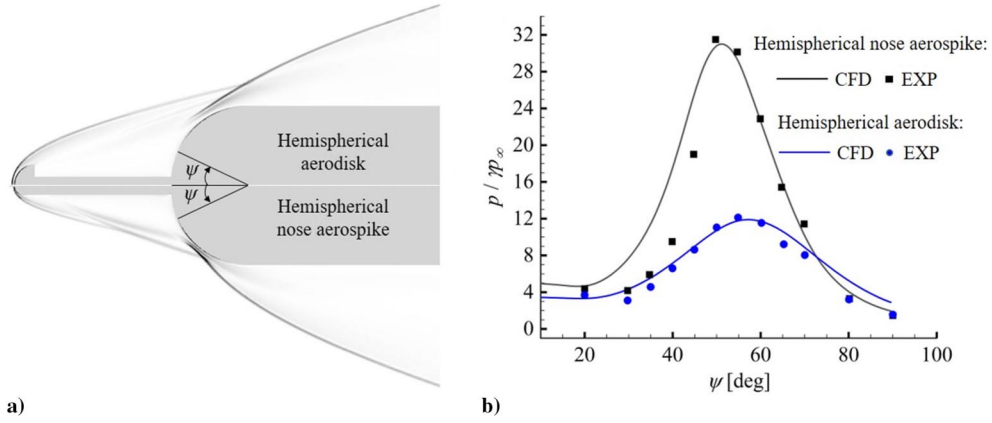


Fig. 6 Hypersonic flow around spikes: a) numerical schlieren of the flowfield; b) comparison of pressure distribution on the hemisphere between computation and experiment.

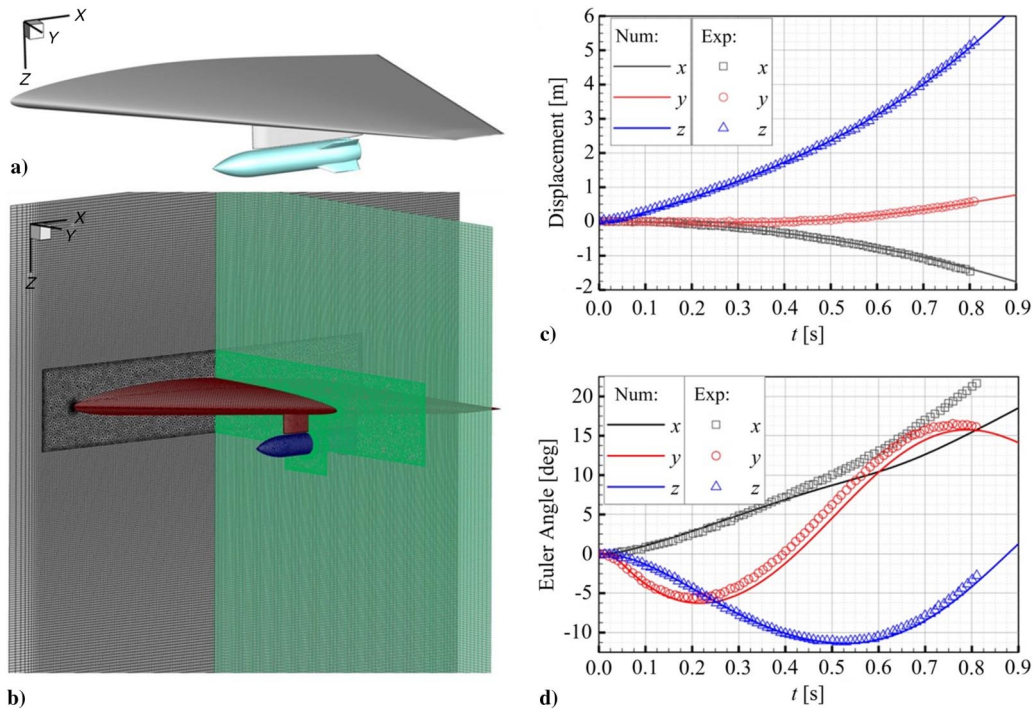


Fig. 7 Wing-pylon-store separation: a) geometry; b) grid. Panels (c) and (d) show the numerical and experimental results of linear and angular displacements of the store, respectively.

study can accurately simulate the complex aerodynamic interference and multibody separation. Also, this method can be applied to predict the stage separation of TSTO vehicles.

IV. Results and Discussion

Four orbiter configurations (i.e., models A, B, C, and D illustrated in Fig. 2c) are employed in dynamic simulation for the LSS of TSTO at AoA = 0, 5, and 8 deg, respectively. Current simulations of LSS assume that the orbiter moves along the upper wall of the booster in the direction of flight and has 6-DOF during separation from the booster. There is a very small clearance between the two stages. The flow physics and aerodynamic characteristics were analyzed in detail, and the numerical schlieren of the flowfield is illustrated by the gradient of density.

A. LSS of Two Stages with Configuration of Model A

1. Aerodynamic Characteristics

Figure 8 presents the axial and normal forces of model A with the displacement of the orbiter during LSS at different AoA cases, as

well as the pitching moment at all levels. In the LSS simulation, the axial direction is in the direction of orbiter motion. A positive value of the moment means the nose-up moment, and vice versa. The expressions of the aerodynamics of both stages are shown in Eqs. (13–15); the “*” is substituted by the “o” and “b” for the calculations of each stage, respectively. The general trend of aerodynamics is almost the same between different AoA. For example, in terms of the orbiter, the slope of the axial force curve increases and reaches a maximum value as the orbiter fairing crosses the leading-edge shock of the booster (i.e., $\Delta x/l_o = 0.925$), and then decreases to zero when separation is complete. Additionally, the axial force increases from the minimum when the orbiter is arranged on the booster to the maximum isolated state after separation. The normal force varies steadily from an initial negative state, then starts to increase when $\Delta x/l_o > 0.925$, and finally decreases to the value of the isolated state. When $\Delta x/l_o = 0.925$, the moment decreases slightly to a minimum, then experiences a peak and valley value as the orbiter separates from the booster, and finally tends to the isolated state. In terms of the booster, the axial and normal forces decrease slightly as the orbiter separates from the booster, especially because the normal force is almost constant during the whole

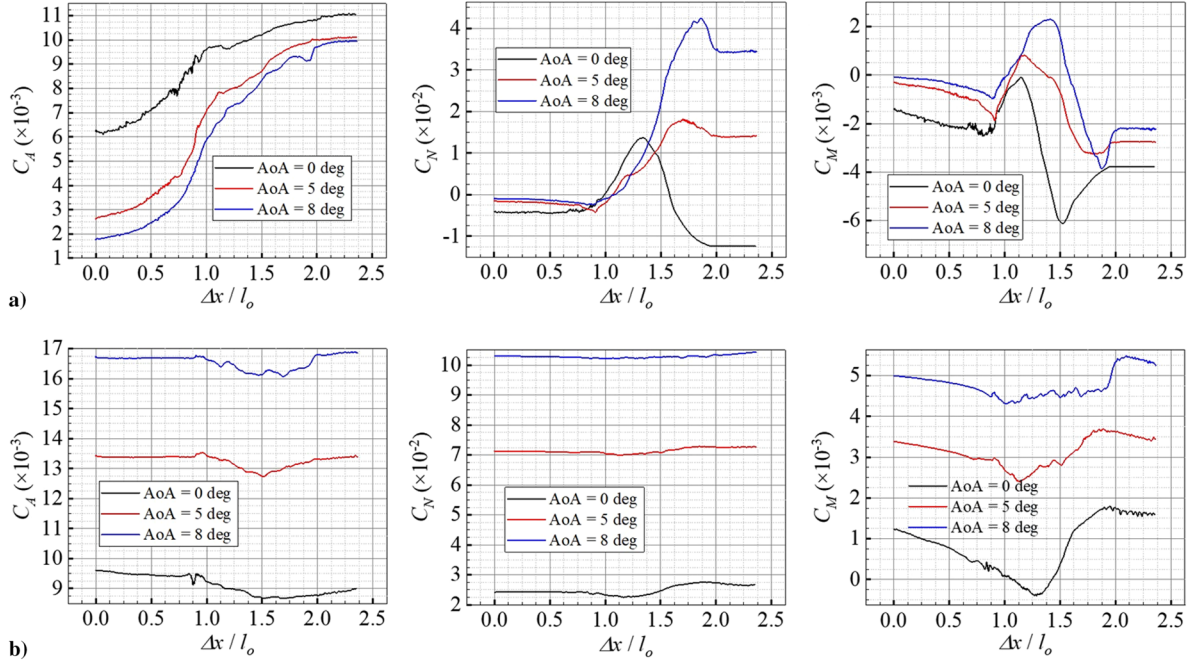


Fig. 8 Aerodynamic characteristics of model A during LSS: a) orbiter; b) booster.

separation. The moment of the booster first decreases monotonously and reaches a minimum during separation, and then gradually increases to an approximate platform value. Moreover, the aerodynamics of the booster fluctuate within a narrow range compared with that of the orbiter, indicating that the influence of aerodynamic interference during separation on the booster is weaker than that of the orbiter. Therefore, the booster can maintain its flight attitude, further ensuring the safety of the stage separation for TSTO. Besides, the computation assumption of the fixed booster during LSS is reasonable.

$$C_A = \frac{A}{(1/2)\rho_\infty U_\infty^2 l_* w_*} \quad (13)$$

$$C_N = \frac{N}{(1/2)\rho_\infty U_\infty^2 l_* w_*} \quad (14)$$

$$C_M = \frac{M_z}{(1/2)\rho_\infty U_\infty^2 l_*^2 w_*} \quad (15)$$

2. Flow Physics

Because the aerodynamic trends are similar between the different AoA cases shown in Fig. 8, those flowfields are also similar. Therefore, the typical flowfield of model A during LSS at AoA = 5 deg and its effects on the aerodynamics of each stage are discussed in this section. The flowfield structures are simpler in LSS than that of the TSS because of the absence of the interstage shock reflection and SBLI, resulting in weak aerodynamic interference in LSS. Figure 9 presents the typical 3-D flowfield structure reflecting the fundamental characteristics of flowfield when the orbiter is positioned on the booster in LSS. Firstly, the conical booster shock S1 attaches on the leading edge of the booster, making the booster to possess a good wave-ride performance at AoA = 5 deg. Secondly, the shear layer S4 develops from the leading edge of the booster and then impinges on the fairing of the orbiter, resulting in a rise in the wall pressure. The supersonic flow above the shear layer encounters the orbiter and induces the formation of the half-conical orbiter shock S2. Thirdly, the developed shear layer S5 with high speed impinges on the tail, brings a pressure rise in the tail, and the tail shock S3 forms and interacts with the shear layer on two sides of the tail. Moreover, the

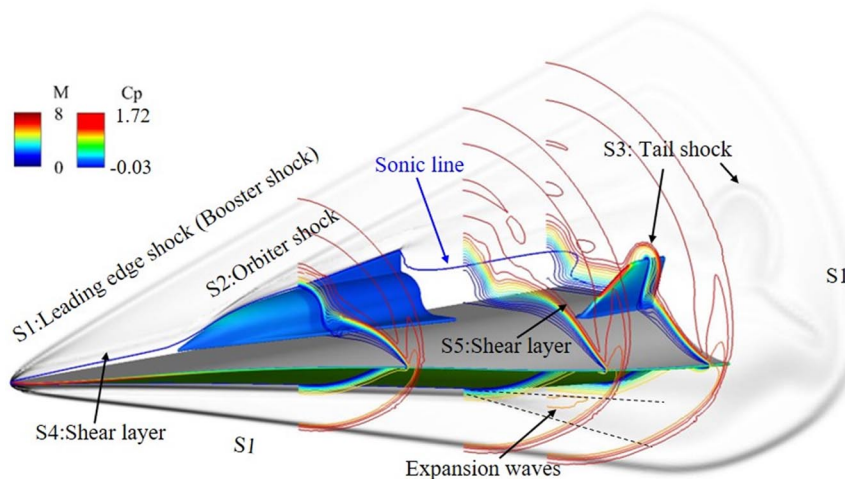


Fig. 9 Flowfield of model A at the instant of $\Delta x/l_o = 0.17$ during LSS when AoA = 5 deg (numerical schlieren at symmetry plane and end plane, and contours of C_p on the two stages, as well as contours lines of Ma).

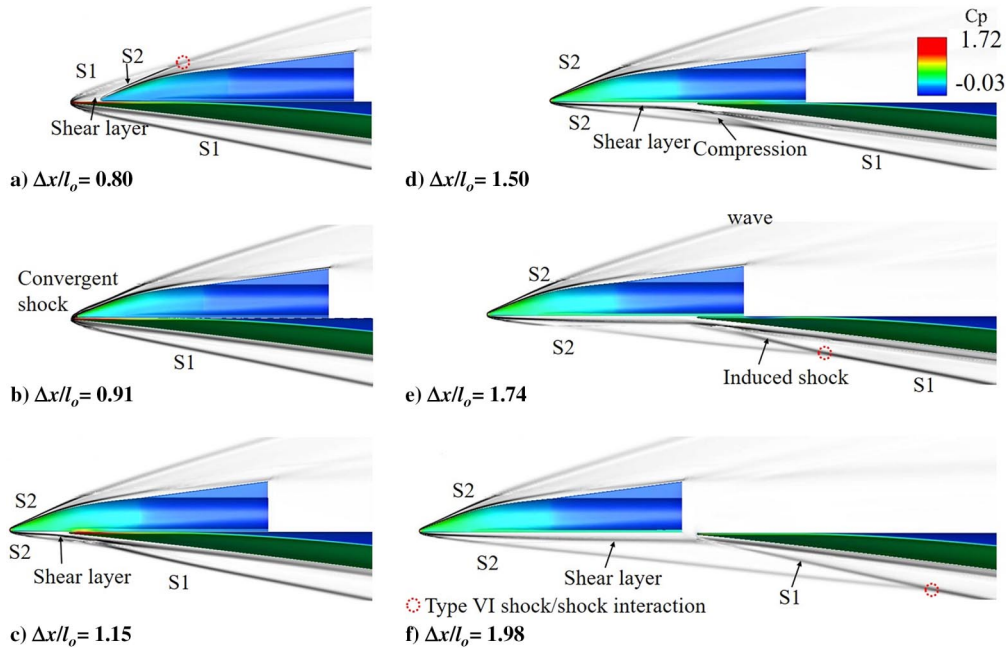


Fig. 10 Flowfields of model A at different instants during LSS when $AoA = 5^\circ$ (symmetry plane of numerical schlieren and contours of C_p on the stages).

subsonic wake flow zone behind the orbiter gradually decreases as the orbiter moves forward.

Figure 10 sketches the pivotal change of the flowfield structure during LSS, which is associated with the aerodynamic variations of each stage. When the orbiter moves to position (a), the interaction position between the shear layer and fairing moves toward the stagnation point, and the strength of the orbiter shock S2 increases because of the increasing shock angle, leading to a further increase in the pressure on the orbiter. Moreover, the booster shocks S1 and S2 occur in the vicinity of the orbiter with type VI SSI (type VI interference occurs when the shocks S1 and S2 cross in a region where they are both weak-oblique shocks from the same family. The corresponding pattern can be founded in the work of Edney [43], who classified the shock interference into six types. The flow organization is simpler than in the other five cases. The interference of type VI in Edney's pattern usually ends up in a shock wave and slip line with expansion waves or very weak oblique shock. Because the type VI SSI in the LSS is too weak that it seems to be ending with a convergent oblique shock wave, other waves are nearly invisible in the numerical schlieren photos. Same below). As a result, the axial force of the orbiter increases faster, and its increment slope reaches a maximum around position (b) when the S1 and S2 converge to a stronger convergent shock. At the same time, the pressure on the orbiter increases. During this process, the moment and normal force of the orbiter decrease (i.e., nose-down moment and negative normal force increase) as the pressure on the nose of the orbiter (including fairing) increases. After that, the axial force increases

slowly. Since the orbiter has broken through the booster shock S1 and encounters the freestream, the normal force and moment increase. The nose-down moment turns to the nose-up and reaches the maximum nearby position (c) $\Delta x/l_o = 1.15$. As shown in Fig. 11a, when $\Delta x/l_o = 1.15$, the orbiter shock S2 impinges on the booster leading edge and interacts with the booster shock S1, generating the diffractive shock. Due to the shock interaction, high pressure is generated on the bottom wall of the orbiter and the upper wall of the booster nearby the leading edge. At $\Delta x/l_o = 1.15$, the nose-up moment of the orbiter reaches a maximum while that of the booster reaches a minimum. In addition, the shear layer or orbiter shock S2 does not impinge on the stagnation point of the booster, as shown in Fig. 10c. Therefore, the axial force of the booster reaches a minimum at $\Delta x/l_o = 1.15$. As the orbiter moves forward, e.g., $\Delta x/l_o = 1.50$ shown in Fig. 11b, the S2 and S1 are almost parallel, so the intensity of SSI is greatly reduced, and the pressure rise near the CG of the orbiter is small. Therefore, the nose-up moment of the orbiter has been changed to the nose-down moment at $\Delta x/l_o = 1.50$. As shown in Fig. 10d, the bent shear layer underneath the booster induces cluster compression waves that converge into the booster shock S1, resulting in type VI SSI between S1 and S2. As the orbiter continues to move, the shear layer directly induces a shock that interacts with the orbiter shock S2 shown in Fig. 10e. Due to the multicompensation effect of the induced shock and S2, the pressure at the bottom of the booster increases, and the axial force of the booster increases from the position $\Delta x/l_o = 1.50$. Moreover, starting from the position $\Delta x/l_o = 1.15$, the zone and intensity of the interstage

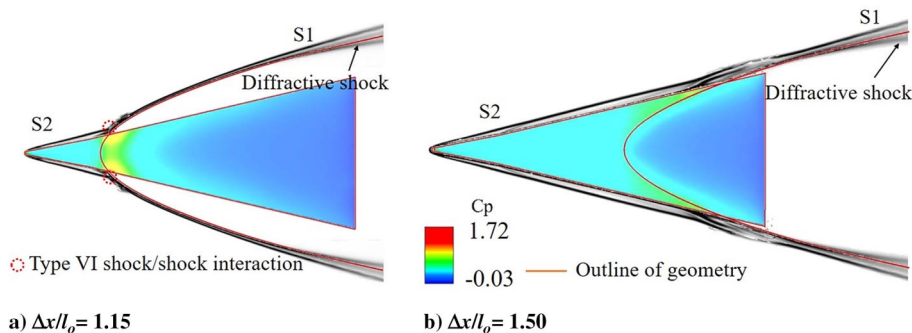


Fig. 11 Numerical schlieren and contours of C_p on the orbiter viewed from the bottom XOZ plane during LSS of model A when $AoA = 5^\circ$.

interference decrease, and thus the high-pressure distribution on the upper wall of the booster narrows, whereas the pressure underneath the nose of the booster increases. The moment of the booster also increases. As shown in Fig. 10e, at $\Delta x/l_o = 1.74$, the interference between two stages locates at the aft body of the orbiter with high-pressure distribution, leading to the maximum nose-down moment of the orbiter. In Fig. 10f, when the orbiter has been separated from the booster, the orbiter turns to an isolated state without the interference of the booster. However, as the interaction between the shear layer of the orbiter and the nose of the booster moves downstream, the high-pressure distribution on the bottom nose of the booster also moves downstream, resulting in the reduction of the nose-up moment of the booster.

B. LSS of Two Stages with Configuration of Model B

Based on the above discussion, the axial force increases rapidly when the orbiter crosses through the booster leading-edge shock because of the convergence of the strong shock S1 and S2, which is detrimental to passenger transport and structural endurance of the orbiter. In addition, the drag reduction may be considered for LSS of the orbiter transport to reduce the fuel and increase its payload. Because using spikes is the simplest and most reliable drag reduction technique, the LSS with different spiked TSTO configurations is considered in this study. The TSTO configuration with half cone spike (model B) is taken as the representative example to gain insight into the aerodynamics and flow mechanism of the LSS of the spiked configuration.

1. Aerodynamic Characteristics

Figure 12 shows the aerodynamic characteristics of models A and B during LSS. As discussed in Sec. IV.A.1, model B shows a similar variation trend of aerodynamics as model A during LSS at different values of AoA. In model B, the aerodynamics of the orbiter exhibits a fluctuation while the spike and fairing pass the leading edge of the booster successively (i.e., $0.577 < \Delta x/l_o < 0.925$), and the normal force and moment of the orbiter show a hump in that phase. The simulation results of model B show the reduced axial force and increased normal force, which leads to an increase in lift-to-drag ratio. Additionally, the spikes increase the moment of the stages at a larger AoA, while having little influence on the axial and normal force of the booster.

2. Flow Physics

Model B is used as a typical spiked configuration to discuss and analyze the flow physics and mechanism during LSS in detail. Figure 13a presents the typical flowfield structure during LSS. As shown in Fig. 13a, the major flowfield difference between the spiked and unspiked configurations is that the shear layer upstream of the orbiter is replaced by a weak shock system. Due to most of the spike being submerged in the shear layer, a weak shock is formed on its tip. The shear layer separates at the tip of the cone, resulting in shear layer S3. The shear layer behind the spike cone attaches to the upper surface of the orbiter. At the same time, the reattachment shock S4 (i.e., orbiter shock) is generated from the reattachment point. Although the effective body defined by the dividing streamline in Fig. 13a is more slender than model A, the axial force is not decreased at the position $\Delta x/l_o = 0.17$, as shown in Fig. 12a. Figure 13b presents the pressure distribution on the upper surface of the orbiter in the case of models A and B. The pressure in the case of model B is slightly higher than that in model A. Because the spike is mostly submerged in the boundary layer of the booster, the reattachment shock S4 formed in the model B case is almost indistinguishable from the orbiter shock S2 in the model A case shown in Fig. 9. Moreover, the pressure on the orbiter and the axial force increases slightly with the compression of the weak spike shock S2. This status will be last until the $\Delta x/l_o > 0.75$. The flow mechanism associated with the spike is very complex and is analyzed in detail below.

Figure 14 sketches the pivotal change in the flowfield structure of TSTO model B during LSS. Before the spike crosses the booster shock S1, the shock system associated with the spike does not change, consisting of the spike foreshock S2, shear layer S3, and reattachment shock S4, as shown in Figs. 14a and 14b. Because the spike crosses the leading edge of the booster, the spike foreshock S2 impinges on the nose of the booster, resulting in a high-pressure rise around the spike and the nose of the booster, as shown in Fig. 14c. At this moment, the normal force and moment of the orbiter reach a maximum because of high pressure on the bottom of the spike. Afterward, the spike foreshock S2 does not impinge on the nose of the booster but interacts with the booster shock S1, as shown in Fig. 14d. As a result, the high pressure on the spike vanishes. When the orbiter moves to position (d), $\Delta x/l_o = 0.77$, diffractive shock is generated due to the booster shock S1 passing through the spike-rod, and the shear layer is lifted along the spike-rod under the interaction of the diffractive shock. The lifted shear layer wraps around the entire

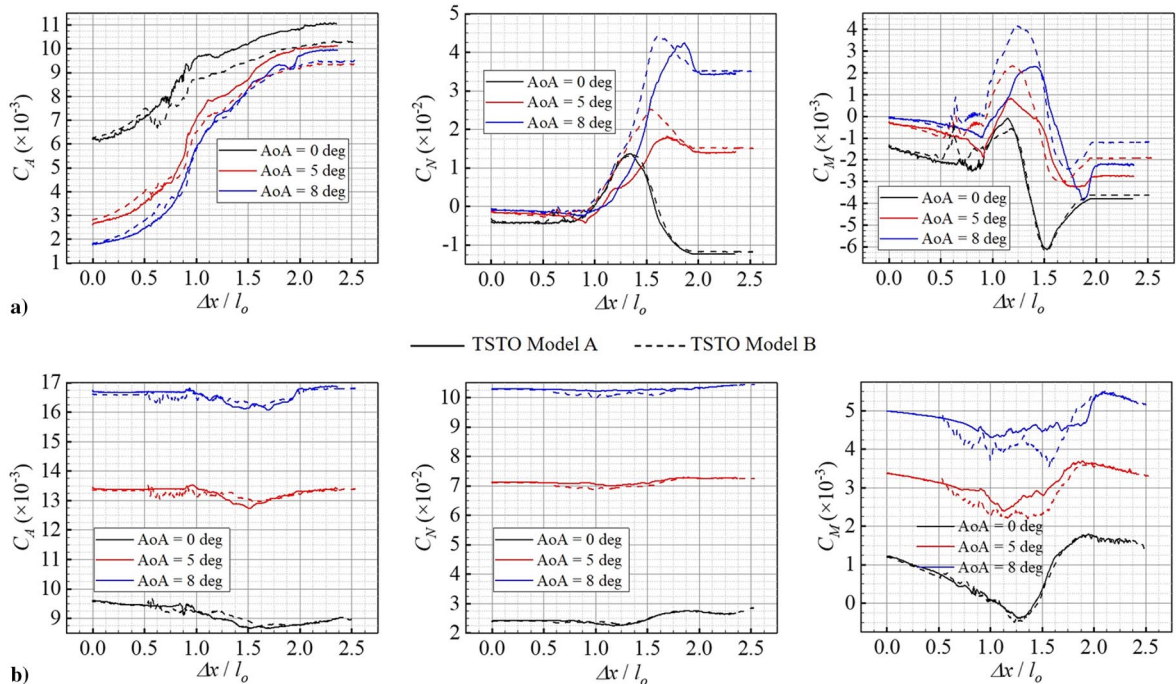


Fig. 12 Comparison of the aerodynamic characteristics between model A (dashed line) and model B (solid line) during LSS: a) orbiter; b) booster.

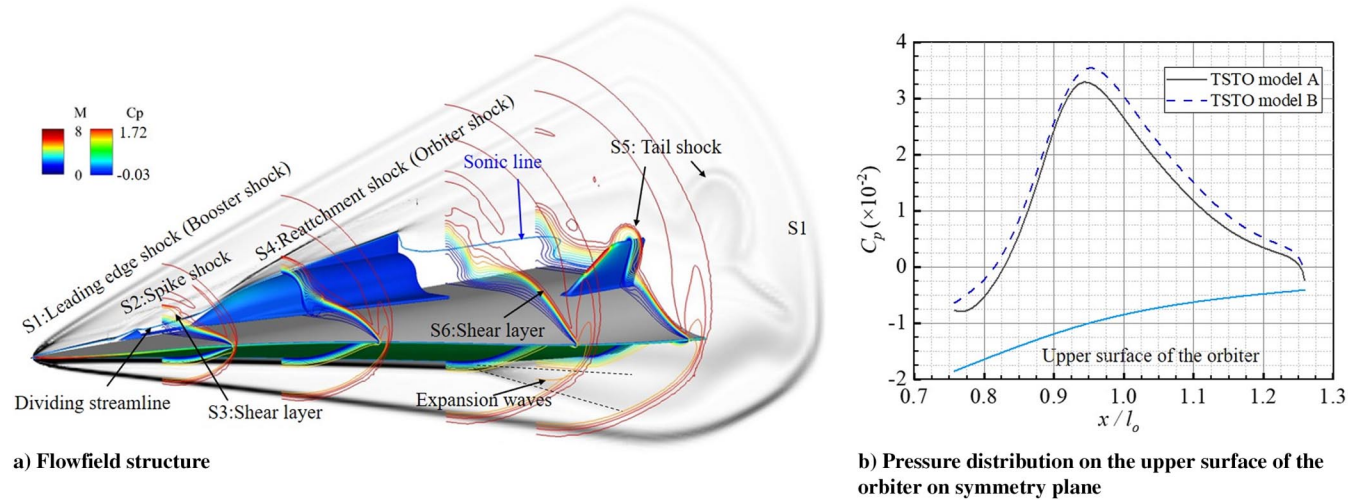


Fig. 13 Flowfield of model B at the instant of $\Delta x/l_o = 0.17$ during LSS when $AoA = 5^\circ$ (numerical schlieren at symmetry plane and end plane, and contours of C_p on the two stages, as well as contours lines of Ma), and comparison of pressure distribution between models A and B.

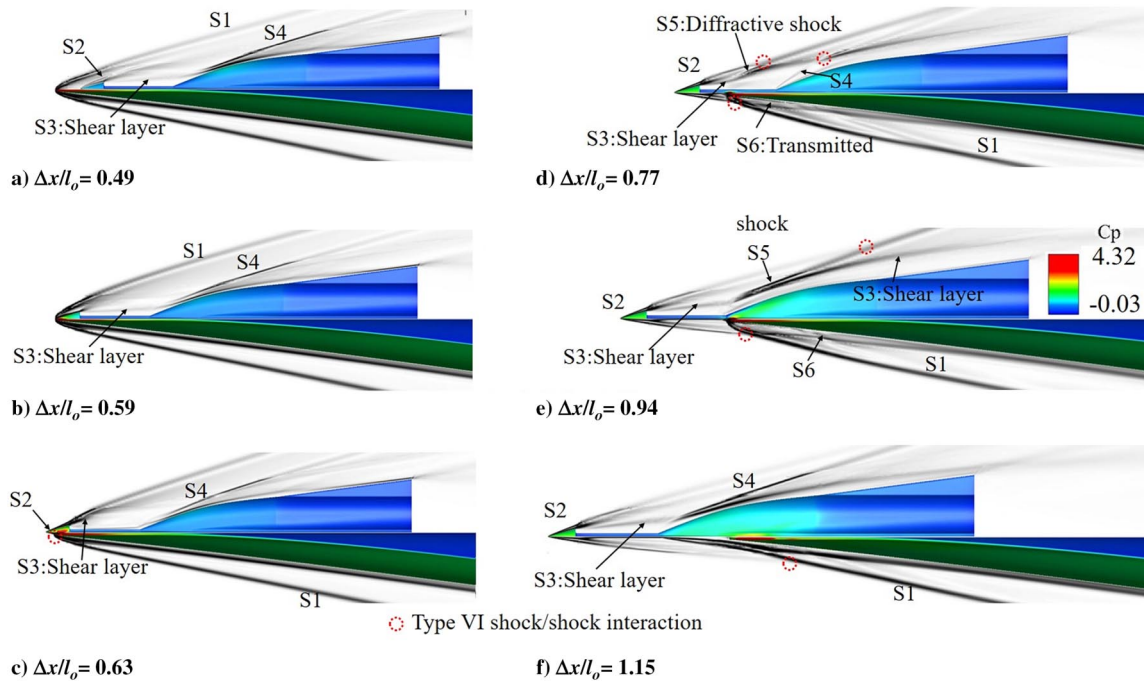


Fig. 14 Flowfields of model B at different instants during LSS when $AoA = 5^\circ$ (symmetry plane of numerical schlieren and contours of C_p on the stages).

orbiter and does not impinge on the nose of the orbiter, generating a very weak orbiter shock S4. As of this moment, the axial force of the orbiter in the case of model B is less than that of the unspiked orbiter. With the orbiter moving forward, as shown in Fig. 14e, the lifted-up shear layer is smoothed by the diffractive shock S5 and approaches the nose of the orbiter. In addition, the spike foreshock S2 interacts with the booster diffractive shock S5 and S1, resulting in the transmitted shock S6. As shown in Fig. 14f, the fairing and nose of the orbiter break through the diffractive shock S5, and the moment of the orbiter begins to increase substantially. Moreover, the stable spike flow structure occurs upstream of the orbiter, and the effective body of the orbiter becomes slender. Figure 12a shows that the axial force is reduced due to the reattachments of the shear layer and weaker orbiter shock S4 on the fairing of the orbiter. Furthermore, except for the additional interaction between the spike foreshock S2 and booster shock S1, the aerodynamic interferences between the two stages are similar to the case of model A as shown in Figs. 10d–10f, and the corresponding variations of aerodynamics are similar too.

C. Comparative Analysis of Spiked Configurations

Given the discussion of Sec. IV.B.1, the effects of the spiked configuration on the aerodynamics of the booster are weaker than that of the orbiter. Therefore, the effects of the spiked configuration on the orbiter are mainly discussed in this section. Figure 15 illustrates the aerodynamics of the orbiter during LSS at $AoA = 5^\circ$ with different spiked configurations. As analyzed in the above sections, spiked configurations play a role in drag reduction. Moreover, the aerodynamic variations between models B and D are almost the same after $\Delta x/l_o > 0.75$ during LSS at $AoA = 5^\circ$. Figure 16 presents the flow structure in the case of model D at the same relative position as the case of model B shown in Fig. 14. Comparing the flow structure of model D and model B, the flow structure changes in both cases are almost the same, indicating that the aerodynamics in both cases are almost the same. However, the aerodynamic difference between model B and D is that the axial force of the orbiter model D is smaller than that of model B before the spike breaks through the booster shock S1. As shown in Fig. 16a, before the spike breaks

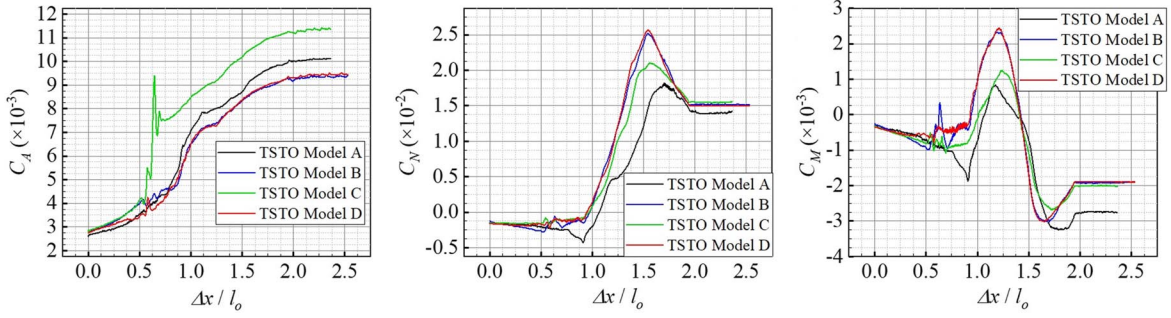


Fig. 15 Aerodynamics of the orbiter during LSS when $AoA = 5$ deg for different TSTO models.

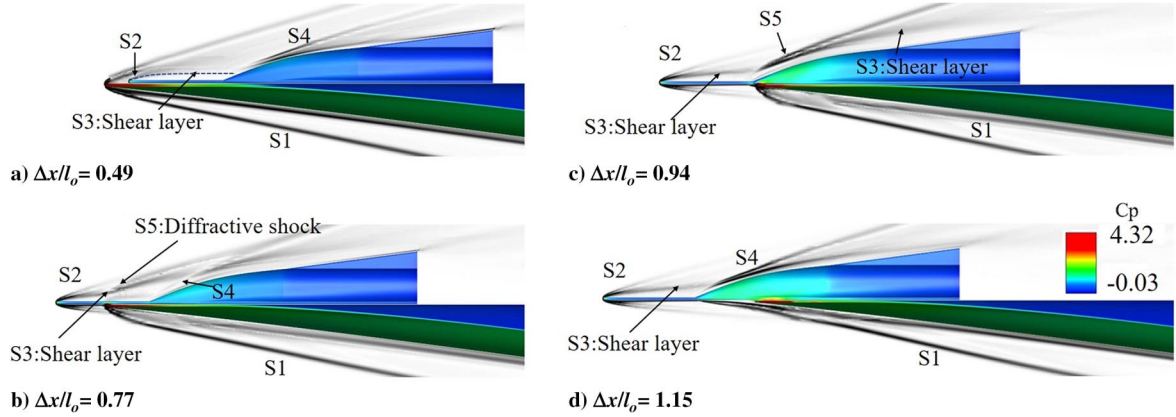


Fig. 16 Flowfields of model D at different instants during LSS when $AoA = 5$ deg (symmetry plane of numerical schlieren and contours of C_p on the stages).

through S1, the partial body of spike model D submerged in the boundary layer of the booster is more than that of the spike model B. Therefore, the spike foreshock S2 of model D is weaker than that of model B, and the axial force of the spiked orbiter D is smaller than that of spiked orbiter B.

As shown in Fig. 15, the axial force of the orbiter in the case of model C is larger than that of the other models during LSS, which increases rather than contributing to the reduction of drag. Moreover, the axial force of the orbiter in the case of model C shows a large

fluctuation when the spike breaks through the booster shock S1. Figure 17 presents the flowfield structures in the case of model C when the spike breaks through the booster shock S1. Before the spike breaks through S1, the flow structure is similar to the other spike model cases discussed previously, as shown in Fig. 17a. However, the major difference between the flow structure in model C and the other models is that a stronger foreshock S2 is generated when the spike breaks through S1. When the orbiter moves to position (b), the supersonic flow passes S2 and impinges on the disk so that the

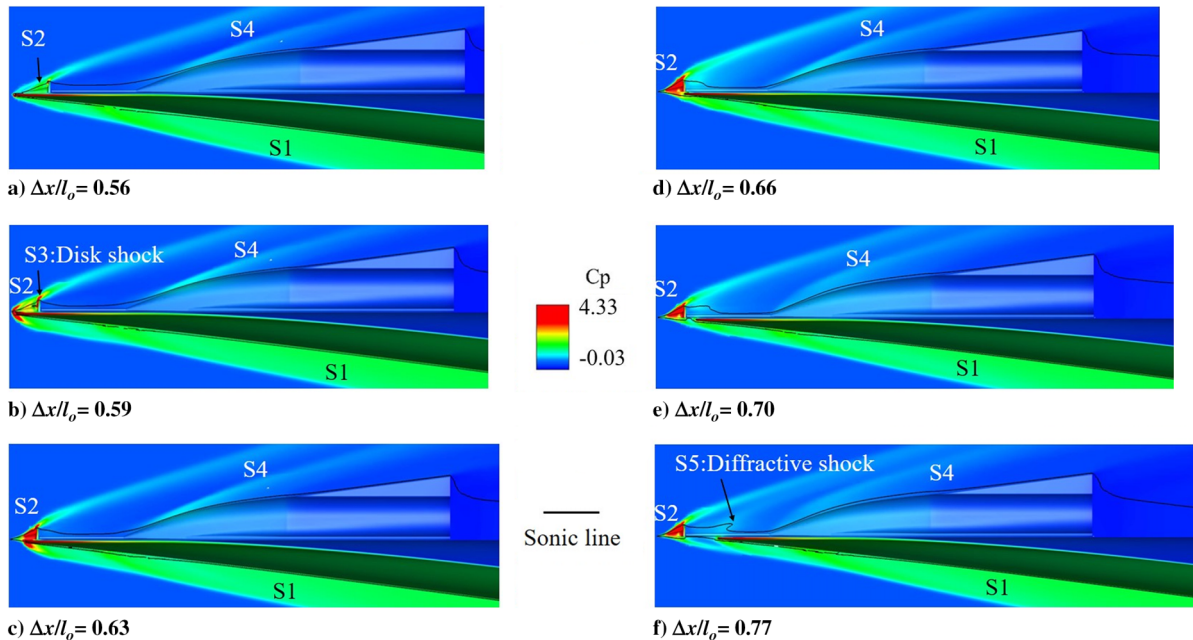


Fig. 17 Flowfields of model C at different instants during LSS when $AoA = 5$ deg (contours of the C_p on the symmetry plane and stages).

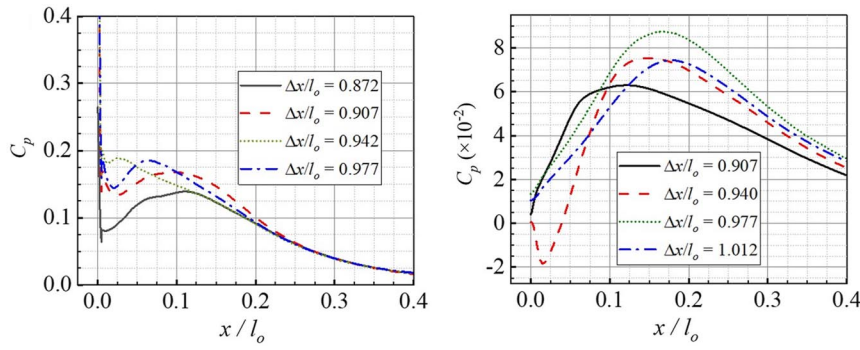


Fig. 18 Pressure distributions on the upper wall of the orbiter in the case of a) model A and b) model B during LSS when AoA = 5 deg.

strong disk shock S3 is generated, which brings the pressure rise on the spike and a rapid increase in the axial force at the first time. As the spike crosses the leading edge of the booster, the pressure around the disk increases, and the sonic line is lifted (i.e., the subsonic zone attached to the cone tends to larger). Moreover, the adverse pressure gradient forms upstream of the disk then propagates upstream to cover the whole cone surface. Finally, a stable recirculation zone attaches upstream of the disk, causing the foreshock S2 to become stronger, as shown in Figs. 17b–17e. In this way, the axial force reaches maximum rapidly. After the spike passes through the leading edge of the booster, the diffractive shock S5 is generated upstream the fairing of the orbiter, and the strength of the orbiter shock S4 is reduced, leading to a decrease in the axial force. The subsequent variations in aerodynamics and flowfields are similar to other spiked models discussed above.

Finally, the problem of rapidly increasing axial force when the orbiter crosses the booster leading-edge shock is also presented in the spiked TSTO model, as shown in Fig. 15. Although the convergent of the orbiter shock and booster leading-edge shock is replaced by the convergent of the reattachment shock (orbiter shock) and the diffractive shock in the LSS of spiked models, the axial force still pulls up at the moment. In addition to the qualitative analysis of the shock structure illustrating the rapid increase in axial force, Fig. 18 shows the pressure distributions on the upper wall of the orbiter at certain moments when the nose of the orbiter breaks through the leading-edge shock of the booster in the cases of models A and B. To compare the changes in C_p distribution between those instants more clearly, the plot of C_p values in Fig. 18a are adapted in the range [0, 0.4], and the maximum of C_p values for those instants are 0.26, 1.16, 1.65, and 1.65, respectively. At these moments, the pressure distributions on the orbiter show a significant rise and fall as the nose shock wave converges and reconstructs. The axial force increases rapidly, and the slope of its increment curve reaches a maximum when the fairing of the orbiter crosses the nose of the booster. In addition, the pressure on the orbiter is less in the case of model B than in model A. In the case of model B, the axial force and the nose-up moment of the orbiter are less than those of model A, and the axial force could experience significant fluctuation in the LSS of model C.

D. Effects of Angle of Attack

As mentioned previously, the general trends of aerodynamics between different AoA cases are almost the same as illustrated in Fig. 12. More specifically, regarding the aerodynamic values of the booster, the range of variation translates upward with increasing AoA, and the fluctuation range does not change significantly. However, the fluctuation range in orbiter aerodynamics increases with the increase of the AoA. In addition, the drag reduction (i.e., the difference of the terminal axial force of the orbiter between the spiked and unspiked TSTO models) does not increase with the increase of the AoA. This result is because the terminal axial force of the orbiter is almost the same except for model C during LSS at a larger AoA. Table 1 shows the terminal axial force of the orbiter (C_A) and corresponding “drag reduction” [i.e., the difference between the

Table 1 Overview of the drag reduction of TSTO during LSS in different AoA cases

Model	AoA = 0 deg		AoA = 5 deg		AoA = 10 deg	
	$C_A (\times 10^{-3})$	DR, %	$C_A (\times 10^{-3})$	DR, %	$C_A (\times 10^{-3})$	DR, %
A	11.1	—	10.1	—	9.9	—
B	10.3	-7	9.4	-7	9.3	-6
C	11.9	7	11.3	12	12.3	24
D	10.7	-4	9.4	-7	9.5	-4

terminal axial force of the spiked orbiter and unspiked orbiter, with $DR = (C_{A,s} - C_{A,o})/C_{A,o} \times 100\%$] of four TSTO models during LSS at different AoA cases. Among all three spike models, the spiked model B has the best drag reduction, reducing the drag by 7% at AoA = 0 and 5 deg. For model D, the drag reduction is best when the AoA = 5 deg, and the drag reduction decreases at other values of the AoA. Model C increases the drag instead of reducing it, and the drag increases with the increasing AoA.

To enhance the results of drag reduction using spike for LSS of TSTO, the performance of the drag reduction of the spiked TSTO models B and D is compared with other studies from the open literature [28,29,40] on the drag reduction for the highly blunted body using spike at supersonic and hypersonic flows, as shown as Fig. 19. Firstly, the drag reduction nearly decreases as the increasing of AoA as presented by the results of the literature as shown by the study of Milicev and Pavlovic [29], and the spike plays a role in increasing the drag at larger AoA as presented by the study of Menezes et al. [28]. Secondly, the performance of drag reduction depends on the spike length to model base diameter, i.e., L/D , because the drag reduction at $L/D = 1$ is more than that at $L/D = 0.5$ from the study of Motoyama et al. [40]. Moreover, the configuration of spike nose also has a significant effect on the drag reduction; for instance, the hemispherical spike plays a role in drag reduction when AoA < 9°, whereas the conical spike increases the drag as shown by the results of Menezes et al. [28]. In addition, the drag reduction of spike for LSS of TSTO in the study is smaller than that for highly blunt body because the blunt degree of the nose of the orbiter is very small compared to the highly blunt body in that literature and the drag reduction performance using spike is not drawn brightly. However, the comparison shows that the spike used on the blunt nose of the orbiter for LSS of TSTO for reducing drag would be significant, which may be studied or demonstrated in future research.

In terms of aerodynamic interference, Table 2 shows the intensity of the aerodynamic interference, which is expressed by the maximum value of difference between interference loads on the orbiter and those of the isolated orbiter. Moreover, the aerodynamic interference is quantified by the expressions of the C_N and C_M of the orbiter: $|\Delta C_N| = |C_N - C_{N,iso}|_{\max}/C_{N,iso}$ and $|\Delta C_M| = |C_M - C_{M,iso}|_{\max}/C_{M,iso}$. From the previous analysis, the value of $|C_N - C_{N,iso}|_{\max}/C_{N,iso}$ in LSS would occur at the initial

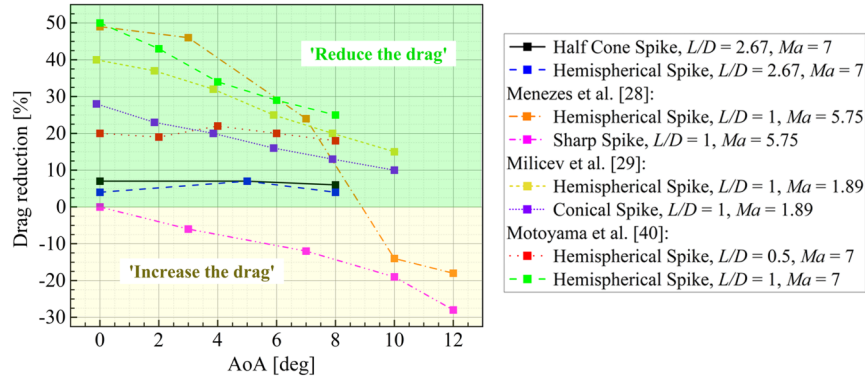


Fig. 19 Comparison of the drag reduction using the spike between this study and other open literature.

Table 2 Overview of the aerodynamic interference intensity of TSTO during LSS for different AoA cases

Model	AoA = 0 deg		AoA = 5 deg		AoA = 10 deg	
	ΔC_N	ΔC_M	ΔC_N	ΔC_M	ΔC_N	ΔC_M
A	-2.11	0.98	1.11	-1.30	1.03	-2.05
B	-2.15	0.89	1.09	-2.20	1.02	-4.52
C	-2.02	0.76	1.10	-1.61	1.03	-3.43
D	-2.03	1.06	1.11	-2.29	1.03	-4.37

phase when the C_N keeps minimum value, i.e., $C_{N,min}$, or at the medium phase when the orbiter is separating from the booster and the C_N changes to a maximum value, i.e., $C_{N,max}$. As the AoA increases, the $C_{N,max}$ tends to the value of $C_{N,iso}$ as shown in Fig. 12a. Moreover, the $C_{N,iso}$ is increasing with the AoA, whereas the $C_{N,min}$ is nearly invariant. Hence, $|\Delta C_N|$ should decrease with the increase of AoA and finally tend to one. For the $|\Delta C_M|$ as function of AoA during LSS, the value of $|C_M - C_{M,iso}|_{max}/C_{M,iso}$ in LSS would occur at the initial phase when the C_M keeps a minimum value, i.e., $C_{M,min}$, or at the medium phase when the orbiter is separating from the booster and the C_N changes to peak value, i.e., $C_{N,peak}$. As the AoA increases, the $C_{M,peak}$ increases with the increase of AoA, whereas the $C_{M,iso}$ decreases with the increase of AoA, as shown in Fig. 12a. Hence, $|\Delta C_M|$ should increase with the increase of AoA. Table 2 also demonstrates that $|\Delta C_N|$ decreases with increasing AoA, whereas the $|\Delta C_M|$ increases as AoA increases. If the interference of the normal force and moment is completely considered, the aerodynamic interference during LSS at AoA = 5 deg is the weakest. Therefore, model A at AoA = 5 deg is favorable of LSS for TSTO. On the other hand, if the drag reduction and aerodynamic interference are altogether considered in LSS of TSTO, model B at AoA = 0 and 5 deg for LSS is preferred.

For comparison of two separation schemes, i.e., TSS presented in the study of literature and LSS presented in the current study, on the issue of aerodynamic interference. The interference types in the LSS are mainly type VI shock/shock interactions with weak effects on the wall pressure rise, whereas those in the TSS are mainly by type I shock/shock interaction, shock wave/boundary-layer interaction caused by shock multiple reflections [10,20,21], and even flow unsteadiness between stages [18,19], resulting in the conceivably severe interference loads on the stages in TSS and troubles for safety separation of TSTO [24]. Hence, the value of LSS for TSTO safe separation is attractive and will be studied further regarding concerns more issued on safety separation.

V. Conclusions

For safety separation of the parallel two-stage vehicle, the numerical simulation and analysis of the dynamic LSS of reference TSTO systems staging at Mach 7 with small interstage clearance, including a waverider and a reusable spaceplane, were

performed to demonstrate and study the simpler and weaker aerodynamic interference compared to that of TSS studied in the literature. Moreover, the drag reduction issues using various spike configurations were addressed. The results are summarized as follows:

- 1) The mechanism of the aerodynamic interference between two stages and the flow structure during LSS with different spike models are clarified and compared. The aerodynamic interference during LSS is simple and weak, which is only associated with type VI shock/shock interference and the convergence of the shock waves. Moreover, the aerodynamic interference during separation is weaker for the booster than for the orbiter, which is beneficial for the safe stage separation of the TSTO.
- 2) The general trends of aerodynamics and the flow structure during the LSS are almost the same between different AoA. When the orbiter shock and leading-edge shock of the booster in the case of the unspiked model (or reattachment shock of the orbiter and diffractive shock of the booster in the case of the spiked model) converge, the axial force increases rapidly.
- 3) The spiked models B and D are effective in drag reduction, whereas the case of model C has the worst performance, which increases axial force during LSS. Moreover, model B has the best performance with a 7% drag reduction.
- 4) The spiked models have better drag reduction when AoA = 5 deg. Spiked model B is favorable in LSS at AoA = 0 and 5 deg because it has good drag reduction and weak aerodynamic interference.

The current study is the first attempt to apply the spike to improve the safe separation of the TSTO vehicle, and some spiked configurations show good performance during the LSS. The future study will focus on the LSS experiment of present TSTO configurations in the hypersonic wind tunnel.

Acknowledgment

This work was supported by the National Natural Science Foundation of China (Grant No. 11672357).

References

- [1] Mehta, U., and Bowles, J., "A Two-Stage-to-Orbit Spaceplane Concept with Growth Potential," 10th AIAA/NAL-NASDA-ISAS International Space Planes and Hypersonic Systems and Technologies Conference, AIAA Paper 2001-1795, 2001. <https://doi.org/10.2514/6.2001-1795>
- [2] Zhou, J., Xiao, Y., Liu, K., and She, W., "Preliminary Analysis for a Two-Stage-to-Orbit Reusable Launch Vehicle," 20th AIAA International Space Planes and Hypersonic Systems and Technologies Conference, AIAA Paper 2015-3536, 2015. <https://doi.org/10.2514/6.2015-3536>
- [3] Zhang, H., Guo, J., Xu, Y., Du, B., Wang, Y., and She, W., "Research on TSTO Reusable Launch Vehicle (RLV) Powered by Turbo-Aided RBCC Engine," 21st AIAA International Space Planes and Hypersonic Technologies Conference, AIAA Paper 2017-2372, 2017. <https://doi.org/10.2514/6.2017-2372>

- [4] Griesemer, P., Mueller, J., and Paluszek, M., "System Design of a Reusable, Horizontal Take-Off/Horizontal Landing Two Stage to Orbit Vehicle," *46th AIAA/ASME/SAE/ASEE Joint Propulsion Conference & Exhibit*, AIAA Paper 2010-7169, 2010.
<https://doi.org/10.2514/6.2010-7169>
- [5] Aso, S., Tani, Y., and Hirayama, T., "Feasibility Study on Shared Design of Hypersonic Transport and Booster of TSTO for Reduction of Development Cost," *2018 AIAA Aerospace Sciences Meeting*, AIAA Paper 2018-0278, 2018.
<https://doi.org/10.2514/6.2018-0278>
- [6] Sorto-Ramos, E., Seyed Alavi, K., and Chudoba, B., "A Parametric Comparison of SSTO and TSTO Space Access Vehicle Concepts," *AIAA Scitech 2020 Forum*, AIAA Paper 2020-0549, 2020.
<https://doi.org/10.2514/6.2020-0549>
- [7] Simon, S., and Chudoba, B., "Conceptual Design and Sizing Study of Reusable TSTO Launch System," *ASCEND 2021*, AIAA Paper 2021-4121, 2021.
<https://doi.org/10.2514/6.2021-4121>
- [8] McKinney, L., Farrell, D., Bogar, T., and Stemler, J., "Investigation of TSTO Propulsion System Options," *14th AIAA/AHI Space Planes and Hypersonic Systems and Technologies Conference*, AIAA Paper 2006-8054, 2006.
<https://doi.org/10.2514/6.2006-8054>
- [9] Dissel, A. F., Kothari, A. P., and Lewis, M. J., "Investigation of Two-Stage-to-Orbit Airbreathing Launch-Vehicle Configurations," *Journal of Spacecraft and Rockets*, Vol. 43, No. 3, 2006, pp. 568–574.
<https://doi.org/10.2514/1.17916>
- [10] Decker, J. P., "Aerodynamic Interference Effects Caused by Parallel-Staged Simple Aerodynamic Configurations at Mach Numbers of 3 and 6," NASA TN D-5379, 1969.
- [11] Moelyadi, M. A., Breitsamter, C., and Laschka, B., "Stage-Separation Aerodynamics of Two-Stage Space Transport Systems Part I: Steady-State Simulations," *Journal of Spacecraft and Rockets*, Vol. 45, No. 6, 2008, pp. 1230–1239.
<https://doi.org/10.2514/1.34828>
- [12] Bordelon, W., Frost, A., and Reed, D., "Stage Separation Wind Tunnel Tests of a Generic TSTO Launch Vehicle," *21st AIAA Applied Aerodynamics Conference*, AIAA Paper 2003-4227, 2003.
<https://doi.org/10.2514/6.2003-4227>
- [13] Murphy, K., Erickson, G., and Goodliff, S., "Experimental Stage Separation Tool Development in Langley's Unitary Plan Wind Tunnel," *22nd Applied Aerodynamics Conference and Exhibit*, AIAA Paper 2004-4727, 2004.
<https://doi.org/10.2514/6.2004-4727>
- [14] Murphy, K., and Scallion, W., "Experimental Stage Separation Tool Development in Nasa Langley's Aerothermodynamics Laboratory," *AIAA Atmospheric Flight Mechanics Conference and Exhibit*, AIAA Paper 2005-6127, 2005.
<https://doi.org/10.2514/6.2005-6127>
- [15] Uematsu, T., Ishida, T., Aso, S., and Tani, Y., "Reduction of Aerodynamic Interference for Separation of Two-Stage Reusable Launch Vehicles," *47th AIAA Aerospace Sciences Meeting including The New Horizons Forum and Aerospace Exposition*, AIAA Paper 2009-1101, 2009.
<https://doi.org/10.2514/6.2009-1101>
- [16] Uematsu, T., Aso, S., and Tani, Y., "Aerodynamic Interference Reduction Method for Two-Stage Launch Vehicles Supersonic Separation," *49th AIAA Aerospace Sciences Meeting Including the New Horizons Forum and Aerospace Exposition*, AIAA Paper 2011-388, 2011.
<https://doi.org/10.2514/6.2011-388>
- [17] Uematsu, T., Aso, S., and Tani, Y., "Supersonic Flight Separation Simulation for TSTO Launch Vehicles Considering Shock Wave Interaction Reduction," *50th AIAA Aerospace Sciences Meeting Including the New Horizons Forum and Aerospace Exposition*, AIAA Paper 2012-0253, 2012.
<https://doi.org/10.2514/6.2012-253>
- [18] Ozawa, H., Hanai, K., Kitamura, K., Mori, K., and Nakamura, Y., "Experimental Investigation of Shear-Layer/Body Interactions in TSTO at Hypersonic Speeds," *46th AIAA Aerospace Sciences Meeting and Exhibit*, AIAA Paper 2008-723, 2008.
<https://doi.org/10.2514/6.2008-723>
- [19] Ozawa, H., Kitamura, K., Hanai, K., Mori, K., and Nakamura, Y., "Unsteady Aerodynamic Interaction Between Two Bodies at Hypersonic Speed," *Transactions of the Japan Society for Aeronautical and Space Sciences*, Vol. 53, No. 180, 2010, pp. 114–121.
<https://doi.org/10.2322/tjsass.53.114>
- [20] Jia, J., Fu, D., and He, Z., "Aerodynamic Interactions of a Reusable Launch Vehicle Model with Different Nose Configurations," *Acta Astronautica*, Vol. 177, Dec. 2020, pp. 58–65.
<https://doi.org/10.1016/j.actaastro.2020.07.022>
- [21] Cheng, J., Chen, R., Qiu, R., Sun, W., and You, Y., "Aerothermodynamic Study of Two-Stage-to-Orbit System Composed of Wide-Speed-Range Vehicle and Rocket," *Acta Astronautica*, Vol. 183, June 2021, pp. 330–345.
<https://doi.org/10.1016/j.actaastro.2020.11.034>
- [22] Brenner, P., "Numerical Simulation of Three-Dimensional and Unsteady Aerodynamics About Bodies in Relative Motion Applied to a TSTO Separation," *5th International Aerospace Planes and Hypersonics Technologies Conference*, AIAA Paper 1993-5142, 1993.
<https://doi.org/10.2514/6.1993-5142>
- [23] Cvrle, T., Breitsamter, C., and Laschka, B., "Numerical Simulation of the Lateral Aerodynamics of an Orbital Stage at Stage Separation Flow Conditions," *Aerospace Science and Technology*, Vol. 4, No. 3, 2000, pp. 157–171.
[https://doi.org/10.1016/S1270-9638\(00\)00132-2](https://doi.org/10.1016/S1270-9638(00)00132-2)
- [24] Liu, Y., Qian, Z., Lu, W., and He, S., "Numerical Investigation on the Safe Stage-Separation Mode for a TSTO Vehicle," *Aerospace Science and Technology*, Vol. 107, Dec. 2020, Paper 106349.
<https://doi.org/10.1016/j.ast.2020.106349>
- [25] Wang, Y., Wang, Y. P., Xue, X. P., and Jiang, Z. L., "Numerical Investigation on Safe Stage Separation Problem of a TSTO Model at Mach 7," *Chinese Journal of Theoretical and Applied Mechanics*, Vol. 54, No. 2, 2022, pp. 526–542.
<https://doi.org/10.6052/0459-1879-21-423>
- [26] Pamadi, B. N., Neirynck, T. A., Hotchko, N. J., Scallion, W. I., Murphy, K. J., and Covell, P. F., "Simulation and Analyses of Stage Separation of Two-Stage Reusable Launch Vehicles," *Journal of Spacecraft and Rockets*, Vol. 44, No. 1, 2007, pp. 66–80.
<https://doi.org/10.2514/1.17896>
- [27] Ahmed, M. Y. M., and Qin, N., "Recent Advances in the Aerothermodynamics of Spiked Hypersonic Vehicles," *Progress in Aerospace Sciences*, Vol. 47, No. 6, 2011, pp. 425–449.
<https://doi.org/10.1016/j.paerosci.2011.06.001>
- [28] Menezes, V., Saravanan, S., Jagadeesh, G., and Reddy, K. P. J., "Experimental Investigations of Hypersonic Flow over Highly Blunted Cones with Aerospikes," *AIAA Journal*, Vol. 41, No. 10, 2003, pp. 1955–1966.
<https://doi.org/10.2514/2.1885>
- [29] Milicev, S. S., and Pavlovic, M. D., "Influence of Spike Shape at Supersonic Flow Past Blunt-Nosed Bodies: Experimental Study," *AIAA Journal*, Vol. 40, No. 5, 2002, pp. 1018–1020.
<https://doi.org/10.2514/3.15157>
- [30] Weingartner, S., "SAENGER—The Reference Concept of the German Hypersonics Technology Program," *5th International Aerospace Planes and Hypersonics Technologies Conference*, AIAA Paper 1993-5161, 1993.
<https://doi.org/10.2514/6.1993-5161>
- [31] Sutherland, W., "The Viscosity of Gases and Molecular Force," *Philosophical*, Vol. 5, No. 36, Dec. 1893, pp. 507–531.
- [32] Menter, F. R., "Two-Equation Eddy-Viscosity Turbulence Models for Engineering Applications," *AIAA Journal*, Vol. 32, No. 8, 1994, pp. 1598–1605.
<https://doi.org/10.2514/3.12149>
- [33] Kurbatskii, K., and Montanari, F., "Application of Pressure-Based Coupled Solver to the Problem of Hypersonic Missiles with Aerospikes," *45th AIAA Aerospace Sciences Meeting and Exhibit*, AIAA Paper 2007-462, 2007.
<https://doi.org/10.2514/6.2007-462>
- [34] Chakravarthy, S., "A Unified-Grid Finite Volume Formulation for Computational Fluid Dynamics," *International Journal for Numerical Methods in Fluids*, Vol. 31, No. 1, 1999, pp. 309–323.
[https://doi.org/10.1002/\(SICI\)1097-0363\(19990915\)31:1<309::AID-FLD971>3.0.CO;2-M](https://doi.org/10.1002/(SICI)1097-0363(19990915)31:1<309::AID-FLD971>3.0.CO;2-M)
- [35] Luo, H., Baum, J., and Lohner, R., "Extension of Hllc Scheme for Flows at All Speeds," *16th AIAA Computational Fluid Dynamics Conference*, AIAA Paper 2003-3840, 2003.
<https://doi.org/10.2514/6.2003-3840>
- [36] Toro, E. F., *Riemann Solvers and Numerical Methods for Fluid Dynamics: A Practical Introduction*, Springer Science & Business Media, New York, 2009, pp. 315–344.
- [37] Edwards, J. R., "An Implicit Multigrid Algorithm for Computing Hypersonic, Chemically Reacting Viscous Flows," *Journal of Computational Physics*, Vol. 123, No. 1, 1996, pp. 84–95.
<https://doi.org/10.1006/jcph.1996.0007>
- [38] Tian, S., Fu, J., and Chen, J., "A Numerical Method for Multi-Body Separation with Collisions," *Aerospace Science and Technology*, Vol. 109, Feb. 2021, Paper 106426.
<https://doi.org/10.1016/j.ast.2020.106426>

- [39] Zaghi, S., Di Mascio, A., Broglia, R., and Muscari, R., "Application of Dynamic Overlapping Grids to the Simulation of the Flow around a Fully-Appended Submarine," *Mathematics and Computers in Simulation*, Vol. 116, Oct. 2015, pp. 75–88.
<https://doi.org/10.1016/j.matcom.2014.11.003>
- [40] Motoyama, N., Mihara, K., Miyajima, R., Watanuki, T., and Kubota, H., "Thermal Protection and Drag Reduction with Use of Spike in Hypersonic Flow," *10th AIAA/NAL-NASDA-ISAS International Space Planes and Hypersonic Systems and Technologies Conference*, AIAA Paper 2001-1828, 2001.
<https://doi.org/10.2514/6.2001-1828>
- [41] Heim, R. R., "CFD Wing/ Pylon/ Finned Store Mutual Interference Wind Tunnel Experiment," AEDC-TSR-91-P4, 1991.
- [42] Snyder, D., Koutsavdis, E., and Anttonen, J., "Transonic Store Separation Using Unstructured CFD with Dynamic Meshing," *33rd AIAA Fluid Dynamics Conference and Exhibit*, AIAA Paper 2003-3919, 2003.
<https://doi.org/10.2514/6.2003-3919>
- [43] Edney, B., "Anomalous Heat Transfer and Pressure Distributions on Blunt Bodies at Hypersonic Speeds in the Presence of an Impinging Shock," Aeronautical Research Inst. of Sweden, FFA Report 115, Stockholm, 1968.

C. Bonnal
Associate Editor